



Experiments and modeling to evaluate global reaction kinetics of three-way catalyst light off for net-zero carbon fuels and selected fuel blends

Austin P. Ladshaw, Sreshtha Sinha Majumdar^{*}, Josh A. Pihl

Oak Ridge National Laboratory, United States

ARTICLE INFO

Keywords:

Three-way catalyst
Stoichiometric light off
Blends
Biofuel
Net-zero carbon fuel

ABSTRACT

Internal combustion engine exhaust composition can have a significant impact on the light-off characteristics of CO, NO, and organics in the three-way-catalyst during cold-start. The U.S. Department of Energy's Co-Optimization of Fuels and Engines initiative was aimed at developing new high-performance fuels, which raises the question of how current three-way-catalysts will perform if the exhaust composition is significantly changed. This work is aimed at quantifying the performance of the catalyst under a variety of different fuel components and mixtures. To this end, a reduced-order model is developed wherein the set of organics examined are placed into molecular groups based on their reactivities and to model each organic within that group with a common kinetic expression. This strategy allows for a first approximation to the light-off characteristics of all organics that fall within that group and to make predictions for fuel blends.

1. Introduction

Emissions control catalysts are critical components for reducing exhaust emissions to meet stringent U.S. E.P.A. regulations. For light-duty (LD), spark-ignition (SI) vehicles, the three-way-catalyst (TWC) is used for the simultaneous conversion of CO, NO_x, and unburned and partially burned fuel species, known as non-methane organic gases (NMOG) [1–7]. While many of the unburned and partially burned fuel species contain oxygen and are therefore not strictly hydrocarbons, this manuscript uses the term hydrocarbons (HCs) as shorthand to refer to all organic species (those containing C, H, and/or O). Numerous combinations of active materials for TWCs have been investigated over the past few decades: (i) noble metals such as Pd/Pt/Rh have been studied extensively as the primary active sites for catalytic conversion [7–14], oxides such as Al₂O₃, CeO₂, and/or ZrO₂ have been used as supporting additives and/or for oxygen storage capacity within the catalyst [12–18], and more recently there have been studies performed with LaFeO₃ (LFOs) materials with non-PGM metals used for catalytically active sites [19–21]. Generally, the Pt/Pd materials with CeO₂ for oxygen storage are the most commonly utilized by industry and most heavily researched [1,5–7,14,22]. Research into TWC performance is very diverse, but can be roughly categorized into: (i) aging impacts on active metals sites and oxygen storage [1,15,23], (ii) lean and/or rich exhaust compositions and the impacts of cycling between each [5,17,

24], and (iii) reducing cold-start emissions [13,25,26].

Aging of a TWC is driven by high temperature and long duration exposure to exhaust gases. It can cause sintering of the noble metals resulting in losses in oxygen storage capacity [1,15,23]. This generally results in a decrease in conversion efficiency over the lifetime of the catalyst.

The operating air/fuel ratio of the engine has a major impact on TWC conversion efficiency of NO_x, CO, and HCs. Air/fuel ratio is often characterized by the dimensionless term λ , which is the ratio between the operating air/fuel ratio and the stoichiometric air/fuel ratio. If the engine runs with excess air ($\lambda > 1$), then exhaust gas entering the TWC has excess oxygen. The presence of excess oxygen, referred to as fuel-lean or lean operation, makes conversion of NO_x over the TWC challenging. If the engine runs with insufficient air to burn all the fuel ($\lambda < 1$), then there will be an excess of CO and HCs. The presence of excess reductants, referred to as fuel-rich or rich conditions, results in challenges for achieving complete conversion of CO and HCs. Simultaneous conversion of NO_x, CO, and HCs is maximized in a very narrow window of λ around the stoichiometric point of the system (i.e., $\lambda = 1$) [1,5,17, 24].

Despite the variations in catalyst performance with aging and lean-rich operation, TWCs generally achieve high conversion efficiencies under normal exhaust operating conditions. However, they are not effective at low temperatures; as much as 80 % of the total emissions released in a full drive cycle may take place immediately after the engine

^{*} Correspondence to: R&D Associate Staff, Oak Ridge National Laboratory.

E-mail address: sinhamajums@ornl.gov (S.S. Majumdar).

Nomenclature

Symbols

$C_{b,i}$	Gas-phase concentrations of species i in the channel space of the monolith (mol/L).
C_i	Gas-phase concentrations of species i in the pore-space of the washcoat (mol/L).
$D_{p,i}$	Pore diffusivity of species i in the washcoat (cm^2/min).
$E_{R,i}$	Inhibition binding energy for CO or HC (J/mol).
G_a	Surface area to volume ratio for the washcoat layer of the catalyst (cm^{-1}).
k_i	Forward rate constant for reaction i (units depend on reaction order).
k_{-i}	Reverse rate constant for reaction i (units depend on reaction order).
$k_{R,i}$	Inhibition adsorption constant for CO or HC (L/mol).
$k_{m,i}$	Effective mass-transfer rate from bulk to pore-space (cm/min).
R	Gas law constant (J/K/mol).
R_{CO}	Inhibition factor for CO (dimensionless).
R_{HC}	Inhibition factor for HCs (dimensionless).
r_i	Overall rate of reaction for i^{th} reaction (mol/L /min).
T	Catalyst temperature (K).
u_{ij}	Molar stoichiometry for the i^{th} species from the j^{th} reaction.
v	Average linear velocity of gases (cm/min).
w_t	Average washcoat thickness (cm).

Greek

ϵ_b	Bulk monolith void space per total volume.
ϵ_w	Volume of washcoat pores per volume of washcoat.

is started (known as cold-start [27–29]. This emphasizes the level of importance in understanding the temperatures that must be achieved in the catalyst in order to minimize the total emissions output of a vehicle. These temperatures are often referred to as light-off temperatures and are typically defined as the catalyst inlet temperature at which a specific level of conversion of a pollutant was achieved (i.e., a T-50 for CO is the temperature at which 50 % conversion of CO occurs) [25,29,30].

Light-off temperatures are extremely sensitive to exhaust gas composition, and can be significantly impacted by the types of HCs used in the fuel [25,29–31]. To that end, the U.S. Department of Energy (DOE) co-optimization of fuels and engines initiative (Co-Optima) has been working towards investigating the impacts that some novel fuel components may have on TWC light-off temperatures [25,29,30]. Previous work in this space has ranged from screening fuel components based on their fuel properties [32] to experimental evaluation of light off of fuel components [29], as well as light off evaluation of fuel blends composed of combinations of those fuel components [30].

The initial work by Majumdar et al. [29] on more than 30 fuel components showed that there was a general trend in reactivity of the different NMOG species based on their chemical structures and functional groups (alcohols, ketones, esters, aromatics, etc.). In this work, that idea is further explored through the development of a reduced order, global kinetics model to quantify reaction kinetics of functional groups with similar catalyst light-off characteristics and to attempt to use that relatively simple model to make predictions on the light-off temperatures of selected fuel blends including net-zero carbon fuels previously investigated in reference [30]. To facilitate the development of this model, an additional set of controlled experiments are performed with synthetic exhaust gases on a flow reactor in the absence of NMOG constituents (i.e., exhaust gases with different combinations of CO, H₂O, CO₂, H₂, and NO all at stoichiometric conditions). This was done to

evaluate the intrinsic kinetics of NO_x and CO light off without interference or inhibition by HCs. Then, the light-off data for each individual NMOG species from reference [29] (summarized in [Supplemental Information](#), Sections D through F) is examined to formulate the kinetics of the HC light off and its impact on the light off of CO and NO. Lastly, the model is used to predict the light-off temperatures of the blends from reference [30] (summarized in [Supplemental Information](#), Sections G through I).

2. Experimental methods

2.1. Catalyst material and aging protocol

The catalyst material used in this study was a core sample from a commercial, dual-zone, Pd/Rh TWC from a 2009 Chevrolet Malibu as previously described in Majumdar et al. [29,30]. The core sample was 2 cm in diameter by 5 cm in length and had an approximate cell density of 600 cpsi (cells per square inch) with an average channel area of 1.07 mm by 1.07 mm (from midpoint to midpoint of the cordierite substrate). The washcoat of the sample ranged from a thickness of 18.5–27.7 μm at the walls of the channels to as much as 83.3–101.2 μm in the corners of the channels. An elemental analysis of the washcoat has been previously provided in Majumdar et al. [29,30].

Prior to experimental evaluation, the sample was hydrothermally aged using a synthetic exhaust gas of CO₂, H₂O, O₂, CO, and H₂. The CO₂ and H₂O were held constant at 10 %, while the other gases were varied to cycle the catalyst between neutral-rich-lean conditions. These cycles were carried out at 800 °C for 50 h as specified in the U.S. DRIVE Oxidation Catalyst Test Protocol.[33] During the redox aging at 800 °C, the thermocouple for measuring the catalyst inlet temperature was placed roughly 1 cm from the front face of the catalyst. Additional details on the aging protocol can be found in Majumdar et al.[29,30].

2.2. Experimental setup

All light-off measurements were performed using a synthetic exhaust flow reactor with a gas-hourly space-velocity (GHSV) of 30,000 h^{−1} based on flows at 1 atm and 0 °C and the total volume of the catalyst core sample. Mass flow controllers from MKS Instruments were used to generate gas flows of the desired composition for each run. Regardless of the gas composition for a particular evaluation, the O₂ concentration was controlled with a mass flow controller such that the inlet λ feeding into the TWC was kept at 0.999 (i.e., approximately stoichiometric) based on the calibration work performed previously in Majumdar et al. [29]. A furnace was placed just upstream of the catalyst to control the inlet temperature during temperature ramping and the catalyst temperature was monitored via three thermocouples located at the upstream (1 cm from inlet face), midpoint (2.5 cm from the front face in the radial central channel), and downstream (1 cm from the exit face) of the catalyst to monitor the gas temperatures. Gas compositions were monitored using a California Analytical Instruments Flame Ionization Detector (FID) hydrocarbon analyzer, an MKS Multigas 2030HS FTIR spectrometer, and a Pfeiffer PrismaPlus quadrupole mass spectrometer. Full details and schematic of the setup are provided by Majumdar et al [29,30].

2.3. Experimental protocol

Prior to each light-off evaluation, the TWC was pretreated at 600 °C under a flow of 10 % CO₂ and 10 % H₂O. After pretreatment, a light down was performed at a ramp rate of 5 °C/min down to a temperature of 100 °C. The light down was always performed with the same gaseous HCs (525 ppm ethene, 500 ppm propene, and 150 ppm propane) in order to ensure that the catalyst would always have the same initial state at the beginning of the light off and to provide a way to track changes in catalyst performance over time. After each light down, the HCs used

during the light down were removed from the feed and the synthetic exhaust mixture including the specific fuel being evaluated was introduced. Light off was performed with constant HC concentration (3000 ppm C₁) at a ramp rate of 5 °C/min from 100 °C to 500 °C. Each light off was performed a minimum of three times to ensure reproducibility.

The feed stream for experiments including HCs during light off was always 13 % H₂O, 13 % CO₂, 0.5 % CO, 0.167 % H₂, 0.1 % NO, and 0.3 % total HCs (on a C₁ basis). The feed O₂ was varied to ensure an air/fuel ratio of 0.999. Full details for individual NMOG fuel evaluations are provided in Majumdar et al. [29] and for fuel blends in Majumdar et al. [30].

The various gas mixtures used in the experiments without HCs are outlined in Table 1. Each run was designed to investigate the kinetics of specific reactions or combinations of reactions within the catalyst while isolating from the impact of HC oxidation. For instance, run 1 was to evaluate the kinetics of the water-gas-shift reaction, since that would be the only conversion reaction occurring under the specified conditions. More details on the reactions involved in each run are outlined in Section 4.1. All runs (except for run 1) included sufficient O₂ to ensure an air/fuel ratio of 0.999.

3. Modeling methods

3.1. Model considerations

Modeling strategies reported for TWCs in the literature are diverse and there does not appear to be a standard approach. Some models are as simple as empirical relationships and/or look up tables [22,34], while others are based on machine learning algorithms [35]. The most common categories of TWC modeling literature fall into 2 groups: (i) global kinetics/inhibition models [6,13,36–41] and (ii) elementary/mechanistic reaction models [3,11,12,42–45].

Generally, the mechanistic models use a network of surface reactions to describe how the catalyst active sites are changing or being occupied during operation [11,42–44]. The kinetic rates at the surface are often a function of the surface coverage of a particular adsorbed species [42,43], and a given adsorbed species may react with any number of gas species to create a branching network of reaction pathways [3,44]. For modeling even a relatively simple gas mixture of a single HC, this may result in 50–60 different reactions that may need to be calibrated for each HC and/or catalyst [42,44].

Without explicitly modeling the occupation of catalyst sites through a complex surface reaction network, the impact of site occupation by a chemical species can be emulated through the use of an inhibition type of model. The inhibition type of model was first conceived by Voltz et al. [46]. The governing idea is that the natural or intrinsic rates of a reaction are inhibited by adsorption of some combination of CO, NO, and/or HCs. Thus, the observed rate coefficient for a particular reaction ($k_{obs,i}$) would be equal to k_i/R_i , where k_i is the intrinsic rate of that reaction and R_i is the inhibition factor that represents the surface occupation by a set of adsorbents [46,47]. The inhibition factor would therefore be dependent on the catalyst materials (i.e., type of catalyst sites), as well as the concentrations of adsorbing species in the gas phase. An inhibition type reaction scheme was adopted for this work to reduce model complexities associated with modeling a full set of surface mediated reactions.

Table 1
Controlled experiments gas mixtures.

Run ID	O ₂ (%)	CO ₂ (%)	H ₂ O (%)	CO (ppm)	H ₂ (ppm)	NO (ppm)
1	0	0	13	5000	0	0
2	0.31	13	13	5000	1670	0
3	0.18	13	13	5000	0	1000
4	0.014	13	13	0	1670	1000
5	0.26	13	13	5000	1670	1000

In the literature, numerous inhibition models seem to use different inhibition terms or expressions without a consistent standard. Voltz et al. [46], as well as Ramanathan and Sharma [40], used a single term that is a function of CO, HC, and NO concentrations. Subramaniam and Varma [47], as well as Dubien et al. [39], used different inhibition terms or combinations of inhibition terms for different reactions. Ma et al. [41] derived a polynomial-like inhibition term based on a series of elementary adsorption steps of specific gas species. Other researchers used observed rates without explicit inhibition terms to study or model conversions under specific gas conditions and temperature ranges. [48,49] In this work, an inhibition factor was applied only to the reduction reactions for NO and would be based on either inhibition effects from CO or from a given HC or set of HCs. This was done to minimize the number of fitting parameters necessary in the analysis and was found to be adequate for modeling TWC conversions under a majority of the experimental conditions in this work. Model equations and specific reactions are discussed in the next section.

3.2. Types of reactions

For any TWC model, there are a number of specific reactions that ought to be considered. These will include: (i) oxidation reactions for CO, H₂, and HCs (reactions 1–3i), (ii) NO reduction by CO (reactions 4–6), (iii) NO reduction by H₂ (reactions 7–9), (iv) water-gas-shift (WGS) and steam reforming reactions (reaction 10–11i), and (v) NO reduction by HCs (reaction 12 i) [12,26,39–41,49]. This is likely the minimal set of reactions that should be considered. There are also N₂O and NH₃ forming reactions that may become important at specific exhaust gas temperatures [1,5,9,21,47]. Table 2 outlines the reactions that were modeled in this work, as well as summarizing the rate expressions used for those reactions

For the reactions in Table 2, each reaction rate expression was assumed first-order with respect to the reactants in that reaction, and the intrinsic rate coefficients (k_i) were each assumed to follow a standard Arrhenius rate law [50]. The inhibition effect of CO on NO reactions (R_{CO}) is applied to each NO reaction, except for NO reduction by HC, which has an inhibition effect by the HC (R_{HC}). Those inhibition terms are defined in Eqs. 1 and 2, which include an adsorption constant ($k_{R,i}$) and binding energy parameter ($E_{R,i}$) to represent the approximate occupation of the species on a catalytic site as a function of temperature. Total inhibition by the HC is taken as the sum of individual inhibition terms for each HC in a fuel mixture. Thus, the most inhibitory HC will

Table 2
Summary of reactions used in the model analysis.

ID #	Reaction	Rate Expression
1	CO + 0.5 O ₂ → CO ₂	$r_1 = k_1 C_{CO} C_{O_2}$
2	H ₂ + 0.5 O ₂ → H ₂ O	$r_2 = k_2 C_{H_2} C_{O_2}$
3i	C _x H _y O _z + (x + (y/4) - (z/2)) O ₂ → x CO ₂ + (y/2) H ₂ O	$r_{3i} = k_{3i} C_{HC_i} C_{O_2}$
4	CO + NO → CO ₂ + 0.5 N ₂	$r_4 = \frac{k_4}{R_{CO}} C_{CO} C_{NO}$
5	CO + 2 NO → N ₂ O + CO ₂	$r_5 = \frac{k_5}{R_{CO}} C_{CO} C_{NO}$
6	2.5 CO + NO + 1.5 H ₂ O → NH ₃ + 2.5 CO ₂	$r_6 = \frac{k_6}{R_{CO}} C_{CO} C_{NO} C_{H_2O}$
7	H ₂ + NO → H ₂ O + 0.5 N ₂	$r_7 = \frac{k_7}{R_{CO}} C_{H_2} C_{NO}$
8	H ₂ + 2 NO → N ₂ O + H ₂ O	$r_8 = \frac{k_8}{R_{CO}} C_{H_2} C_{NO}$
9	2.5 H ₂ + NO → NH ₃ + H ₂ O	$r_9 = \frac{k_9}{R_{CO}} C_{H_2} C_{NO}$
10	CO + H ₂ O ↔ CO ₂ + H ₂	$r_{10} = k_{10} C_{CO} C_{H_2O} - k_{-10} C_{CO_2} C_{H_2}$
11i	C _x H _y O _z + (x - z) H ₂ O → x CO + (x + (y/2) - z) H ₂	$r_{11i} = k_{11i} C_{HC_i} C_{H_2O}$
12i	C _x H _y O _z + (2x + (y/2) - z) NO → x CO ₂ + (y/2) H ₂ O + (x + (y/4) - (z/2)) N ₂	$r_{12i} = \frac{k_{12i}}{R_{HC}} C_{HC_i} C_{NO}$

have the greatest inhibition effect on NO reduction. During model development, in all cases it was assumed that there was no inhibition, unless the fitness of the model could be significantly improved by its inclusion.

$$R_{CO} = 1 + k_{R,CO} \bullet \exp\left(-\frac{E_{R,CO}}{RT}\right) \bullet C_{CO} \quad (1)$$

$$R_{HC} = 1 + \sum_{vi} k_{R,HC_i} \bullet \exp\left(-\frac{E_{R,HC_i}}{RT}\right) \bullet C_{HC_i} \quad (2)$$

3.3. Governing equations

The governing equations for a TWC model include: (i) mass and energy balances on the gas phase and catalyst material, along with (ii) mass and heat transfer to and from the gas and solids, as well as (iii) heat transfer at the outer walls [34,38,40,41,50,51]. The mass balance can be described by Eqs. 3 through 5 below, where Eq. 3 is the mass balance in the bulk channel spaces of the monolith catalyst, Eq. 4 is the mass balance in the pore-spaces of the washcoat, and Eq. 5 is the boundary condition for mass transfer from the bulk channel spaces to the pore-space of the washcoat. In these equations, ε_b is the ratio of bulk channel volume to total volume, $C_{b,i}$ is the concentration of the i^{th} species in the bulk space, v is the average linear velocity of the gas through the channel, G_a is the ratio of washcoat outer surface area to catalyst volume, $k_{m,i}$ is the mass transfer rate, C_i is the concentration of the i^{th} species in the pore-space, ε_w is the washcoat porosity, $D_{p,i}$ is the pore diffusivity of the i^{th} species in the washcoat, u_{ij} is the molar contribution to the mass balance on the i^{th} species from the j^{th} reaction, r_j is the reaction rate of the j^{th} reaction in moles per volume of catalyst per time, w_t is the average thickness of the washcoat, z is the axial position along the monolith, and x is the position in the washcoat from 0 at the inner most position and w_t at the outer most position.

$$\varepsilon_b \frac{\partial C_{b,i}}{\partial t} + \frac{\partial}{\partial z} \bullet (\varepsilon_b v C_{b,i}) = -(1 - \varepsilon_b) G_a k_{m,i} (C_{b,i} - C_i|_{x=w_t}) \quad (3)$$

$$\varepsilon_w (1 - \varepsilon_b) \frac{dC_i}{dt} = \frac{\partial}{\partial x} \bullet \left(\varepsilon_w (1 - \varepsilon_b) D_{p,i} \frac{\partial C_i}{\partial x} \right) - \sum_{vj} u_{ij} r_j \quad (4)$$

$$k_{m,i} (C_{b,i} - C_i|_{x=w_t}) = \varepsilon_w D_{p,i} \frac{\partial C_i}{\partial x} \Big|_{x=w_t} \quad (5)$$

For the monolith sample used in this study, an approximate ε_b of 0.775 was measured based on the total open channel size relative to the full cross-sectional area of the 2 cm diameter sample. The washcoat was assumed to have a porosity of 0.4, which is an approximate median value based on reported porosities for similar materials [11,38]. Average washcoat thickness (w_t) and area-to-volume ratio (G_a) were calculated from relationships with cell density, channel size, and hydraulic diameter that are summarized in the Supplemental Information of Ladshaw and Pihl [50]. Mass transport and mass transfer parameters v , $k_{m,i}$, and $D_{p,i}$ were calculated based on the GHSV, as well as relationships with the Sherwood number and molecular diffusivities. These calculations are also summarized in the Supplemental Information of Ladshaw and Pihl [50].

Generally, the mass balance for the TWC would be coupled with an energy balance to describe how the catalyst heats up as a function of the reactions taking place, as well as heat transfer with the outer walls. This would provide a temperature profile along the length of the domain that would impact the relative rates at which each reaction occurs. In this study, however, it was opted to forgo the inclusion of the energy balance in the model analysis and instead directly use the temperature profiles measured along the length of the catalyst using the thermocouples described in Section 2.2 and in Majumdar et al. [29,30]. Thus, for all simulation cases, we have an imported temperature profile that comes directly from the observations of the three thermocouples in the catalyst.

This was done to simplify the model analysis for this study. In General, the simulation framework that the model in this study was built on does include information on constructing energy balances for the domain of interest. That information can be found in the User's Guide distributed with the source code [52].

The decision to remove the need for the energy balance was made for a number of reasons. First, the scope of this model analysis is limited to the parameterization of the kinetic rates of reactions and evaluation of those rates relative to different structural groups of HCs; the focus was not to calibrate for thermal impacts of the wall cooling of the catalyst. Second, each of these reactions already have known reaction enthalpies from a thermodynamics point of view; thus, there is no need to find the heats of reactions, as they can already be found in literature [38,53]. Lastly, directly using temperature profiles from the thermocouples will eliminate uncertainties associated with unknown heat transfer coefficients, wall temperatures, and ambient temperatures, since these were not measured at the time the experiments were performed. While the catalyst sample was contained in an insulated tube, ambient and wall temperatures were not controlled in the experiments, nor were they measured; thus, the heat losses to the outer walls is not accurately known and could introduce significant uncertainty.

3.4. Numerical methods

The source code for the model developed in this work is available at a public GitHub repository [52]. It is built on the Multiphysics Object-Oriented Simulation Environment (MOOSE) open-source project developed by Idaho National Laboratory [54]. The axial dimension of Eq. 3 was discretized using Discontinuous Galerkin finite elements [55], and the washcoat dimension was discretized using finite differences. This creates a hybridization of finite elements and finite differences wherein the washcoat space is represented by a set of functions that simulate diffusion into the pore-spaces within each individual element (or axial position) of the finite element mesh. Additional details of this approach are provided in Supplemental Information (Section A). Numerical solutions to the model were obtained iteratively using a Jacobian-Free Newton-Krylov method [56] and the kinetic parameters were determined using least-squares fitting of the model with the Interior Point Optimization (IPOPT) library [57]. More details on solver methods/options and preconditioning can be found in the User's Guide distributed with the source code [52].

4. Results and discussion

4.1. Kinetics evaluation without hydrocarbons

The simplified mixture experiments performed in this work (summarized in Section 2.3 and Table 1) were used to calibrate for the intrinsic kinetics and CO inhibition factors of reactions that only involve NO, CO and H₂ from Table 2. This includes reactions 1, 2, and 4 through 10. Each of the simplified mixture experiments (runs 1 through 5 from Table 1) was utilized to isolate certain subsets of those reactions so that other reactions could be neglected for a particular analysis. Then, in subsequent analyses, previously determined kinetics would be held

Table 3
Summary of Reaction Rates Determined from Each Controlled Experiment.

Run ID	Reaction to Calibrate	Notes
1	10	Only involves water-gas-shift (WGS)
2	1 and 2	Includes WGS and allows recalibration (if needed)
3	4 through 6	NH ₃ and N ₂ O formed deconvolutes each Includes reaction 1 and 10 (no recalibration)
4	7 through 9	NH ₃ and N ₂ O formed deconvolutes each Includes reaction 2 (no recalibration)
5	Eq. 1	Determines inhibition effect of CO on NO

constant so that other rate terms could be determined. Table 3 outlines which experimental run was used for which set of rate determinations.

The results and comparison between experimental data and model analysis for runs 1 and 2 (from Tables 1 and 3) are provided in Fig. 1. The calibrated rate parameters for reactions 1, 2, and 10 are provided in Supplemental Information (Section B). Simulated profiles for CO and H₂ oxidation, as well as the water-gas-shift reaction describe the data very well. The calibrated parameters for these reactions are held constant for all subsequent analyses of the data sets.

The results from experimental run 3 (CO + NO reactions in the presence of O₂) are shown in Fig. 2. The rates for CO oxidation (reaction 1) and WGS (reaction 10) are held constant in this simulated case so that any additional CO conversion, beyond what is caused by just reaction 1 and 10, is caused by the reactions between CO and NO (reactions 4 through 6). Similarly, the NO conversion observed is the summation of conversion from reactions 4 through 6 (Table 2). In general, for all experimental runs analyzed in Section 4.1, differentiation between how much each reaction contributes to the overall NO conversion versus the formation of other nitrogen by-products the exit concentrations for N₂O and NH₃ were also monitored (Supplemental Information, Section C). Thus, by calibrating the rates of reaction for reactions 5 and 6 (N₂O and NH₃ formation), it can be determined that any residual NO conversion must be the result of reaction 4. However, for the experimental run 3, the model predicts little or no N₂O being formed (Supplemental Information, Figure C1). This is primarily a consequence of the optimization routine, which seeks the minimization of the model result against all the data based on the Euclidean norm. Since the N₂O formation seen is brief and low in magnitude compared to other data sets, it is more likely to be deprioritized in the overall fitness of the model. This is not the case for the subsequent data sets, however, since much more N₂O formation is observed.

Results from experimental run 4 (Figs. 3b) and 5 (Fig. 3a) for NO conversion are plotted together on Fig. 3. The observations for experimental run 4 (i.e., H₂ + NO reactions without CO) are used for the calibration of reactions 7 through 9 in the absence of the inhibition factor induced by CO (i.e., $R_{CO} = 1$ for all reactions in experimental run 4). As before, the differentiation between amount of NO converted to N₂O, NH₃, and N₂ is done by utilizing the observed formations of N₂O and NH₃. Both the data and the model show that we have a nearly complete conversion of NO by H₂ across the full range of temperatures in the absence of CO (Fig. 3b), however, a substantial portion of that apparent NO conversion is from N₂O formation (Fig. 3b). This N₂O formation occurs at some temperature lower than 100 °C and must be kinetically very fast since no N₂O was introduced upstream. Thus, the

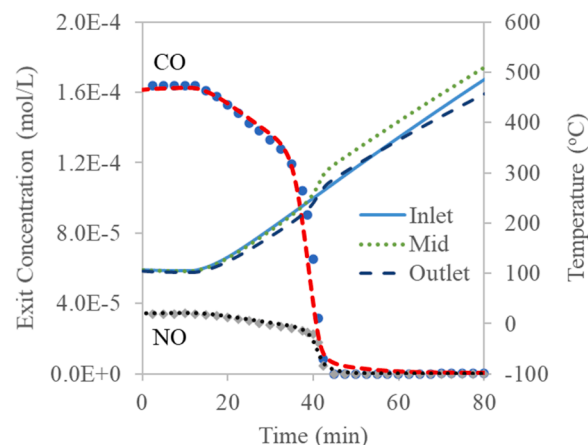


Fig. 2. Simulated CO (red-dashed) and NO (black-dotted) vs the measured CO (blue-circles) and NO (grey-diamonds) for experimental run 3 (CO oxidation + CO/NO reactions).

N₂O seen at the exit of the catalyst all occurred within minutes of NO and H₂ being introduced.

When CO is introduced in experimental run 5 (Fig. 3a), both the model and data demonstrate a significant loss in low temperature conversion of NO compared to the same experiment without CO (Fig. 3b). This loss of conversion is caused by the inhibition of CO on NO reactions and is quantified in the model through Eq. 1. For this last experimental run, all reactions identified in Table 3 are active in the model and the only parameters that are adjusted are the inhibition model parameters from Eq. 1. All kinetic parameters used for all of these experiments are summarized in Supplemental Information, Section B.

In Fig. 3, there are some interesting conversion features in the behavior of NO. Just before the 40 min mark (between about 190 and 220 °C, or 463 and 493 K) there is a short plateau in the NO profile for experimental run 5 (Fig. 3a). At this plateau, there is a transitional period from the partial reduction of NO to N₂O, to the complete reduction of NO to N₂. Thus, this plateau is aligned with the loss of NO conversion from the decrease in N₂O formation (Fig. 3a).

In experimental run 4 (Fig. 3b), there is a similar observed inflection in the NO profile around the same time and temperature window. Both the data and the model show this secondary bump in the conversion profile, thus we can infer that it likely has some physical-chemical meaning. As with experimental run 5 (Fig. 3a), it is probable that

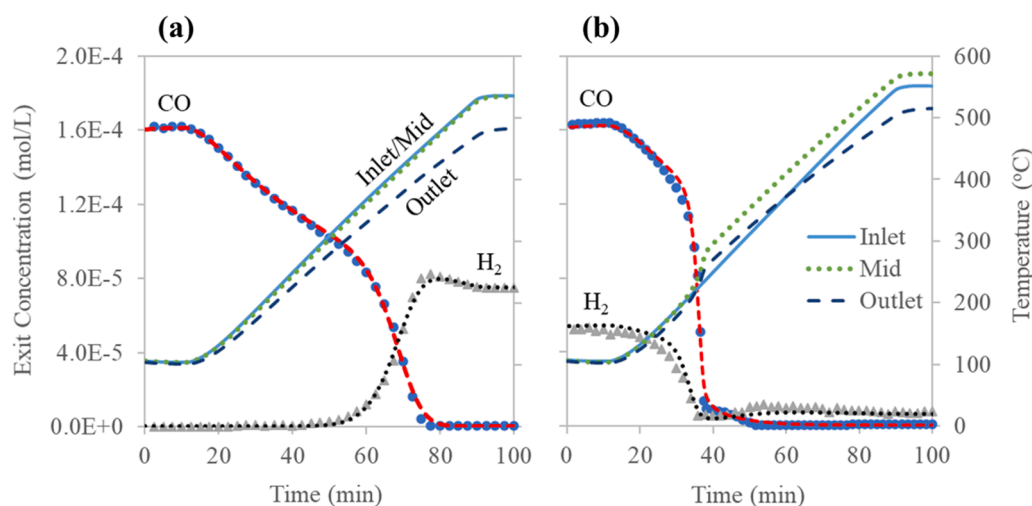


Fig. 1. Simulated CO (red-dashed) and H₂ (black-dotted) vs the measured CO (blue-circles) and H₂ (grey-triangles) for (a) experimental run 1 (WGS only) and (b) experimental run 2 (oxidation + WGS).

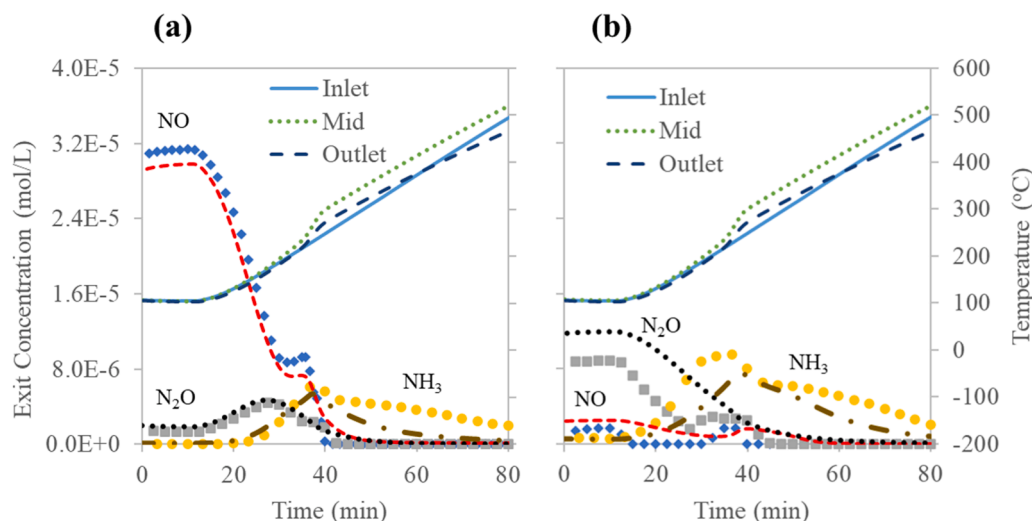


Fig. 3. Simulated NO (red-dashed), N₂O (black-dotted), and NH₃ (brown-dash-dotted) vs the measured NO (blue-diamonds), N₂O (grey-squares), and NH₃ (yellow-circles) for (a) experimental run 5 (H₂ + NO + CO) and (b) experimental run 4 (H₂ + NO without CO).

most of the H₂ has been consumed at this point, which would explain why there is a small loss of NO conversion, but beyond this point the NO conversion appears fully complete. This may be caused by the competing effects between NH₃ formation (reaction 9) and N₂ formation (reaction 7). Since NH₃ formation requires more H₂ than the N₂ formation, the depletion of H₂ will have a greater impact on that reaction, resulting in a decline in both NO utilization and NH₃ formation. As the temperature increases, the rates for N₂ formation become much more significant and allow for more complete NO conversion.

4.2. Kinetics evaluation with pure hydrocarbons

With kinetics associated with reactions 1, 2 and 4 through 10 determined via independent analysis of the experiments in Section 4.1, the remaining reactions associated with the HCs (reaction 3i, 11i, and 12i) can be determined using experimental data from Majumdar et al. [29]. For this analysis, all previously determined reaction rates (reactions 1 and 2, and reactions 4 through 10) are fixed and only the parameters associated with reactions 3i, 11i, and 12i are allowed to vary. Additionally, the set of HCs examined with this model are placed into molecular groups based on the conclusions from Majumdar et al. that molecules with similar chemical structures exhibit similar catalytic reactivities [29]. In each of these groups, the kinetic parameters for the reactions (3i, 11i, and 12i) are all the same within that group. Mechanistically, this would be akin to each molecule within that group having the same rate controlling step within their overall reaction pathway. The exception to that rule is the Alkenes ≤ 3 C (i.e., ethene and propene), which displayed very different reactivities compared to longer chain alkenes and to each other [29]. Table 4 provides the group names and the NMOGs/HCs placed into that group. It is worth noting that methane

Table 4
Summary of Molecular Groups Examined.

Molecular Group	NMOGs in Group
Alcohols: >C3	iso-butanol, n-butanol
Alcohols: \leq C3	ethanol, 2-propanol, 1-propanol
Alkanes: Branched	2-methylpentane, iso-octane
Alkanes: Cyclic	methylcyclohexane, methylcyclopentane
Alkanes: Linear	n-heptane, n-octane
Alkenes: >C3	1-octene, 1-hexene, diisobutylene
Alkenes: \leq C3	ethene, propene
Aromatics	toluene, mesitylene, m-xylene, anisole
Esters	ethylacetate, butylacetate, iso-butylacetate
Ketones	2-butanone, 2-pentanone, methylisobutylketone

and propane were also examined with this model but are not shown in the proceeding plots as their light-off temperatures are off scale due to their low relative reactivities. Information for these HCs can be found in Supplemental Information, Sections D through F.

Optimal kinetic parameters for all NMOGs for reactions 3i, 11i, and 12i are in Supplemental Information, Section D. All transient simulations were carried out for each molecular group (except for Alkenes ≤ 3 C) in order to find a single set of optimal kinetic parameters that could describe the light-off characteristics of all NMOGs within that group. The full set of transient simulation cases and the transient data are provided in Supplemental Information, Section E (and provided in alphabetical order). In most cases examined in this work, it was found that a single set of kinetic parameters to describe the light off of each group was sufficient.

Comparisons between the modeled T-50 s and T-90 s for NMOG, CO, and NO are provided in Figs. 4 through 6. Note that only the T-90 s are shown for NO conversion because the plateau or conversion loss of NO (demonstrated in Fig. 3) at the lower temperatures makes it such that the conversion of NO would cross back and forth over the 50 % conversion mark, thus creating significant uncertainty in what should be considered the T-50 for NO conversion. In Figs. 4 through 6, only a few error bars are shown, which represent the maximum observed standard deviations in any observation. This was done primarily to reduce the amount of clutter on each plot. All standard deviations are recorded in the tables in Supplemental Information, Section F.

The model describes nearly all of the data very well, with a few notable exceptions. While the NMOG, NO, and most of the CO light-off temperatures are generally modeled within ± 10 °C of the observations for each molecular group, the CO light off is not captured very well for large Alkenes (those with more than 3 carbons), and even some of the Aromatics for the T-90 s (Fig. 5). Similar trends for these HCs have been observed in Patterson et al. [58] which showed that heavier species, such as aromatics and large alkenes, push the T-50 light-off to much higher temperatures. However, the light-off curves from Patterson et al. [58] did not show a pronounced “shoulder” feature in the CO light-off, as shown in Fig. 7.

The model is missing the development of a “shoulder” feature in the CO conversion profile that only appears for a few HC species and/or groups, specifically the larger Alkenes, Aromatics, and propene (Fig. 7). This shoulder feature cannot likely be explained just as an inhibition effect. The impact of HC inhibition on CO light off would be strongest at the lower temperature regime (i.e., when the adsorption binding strength and HC concentrations are the highest), then become

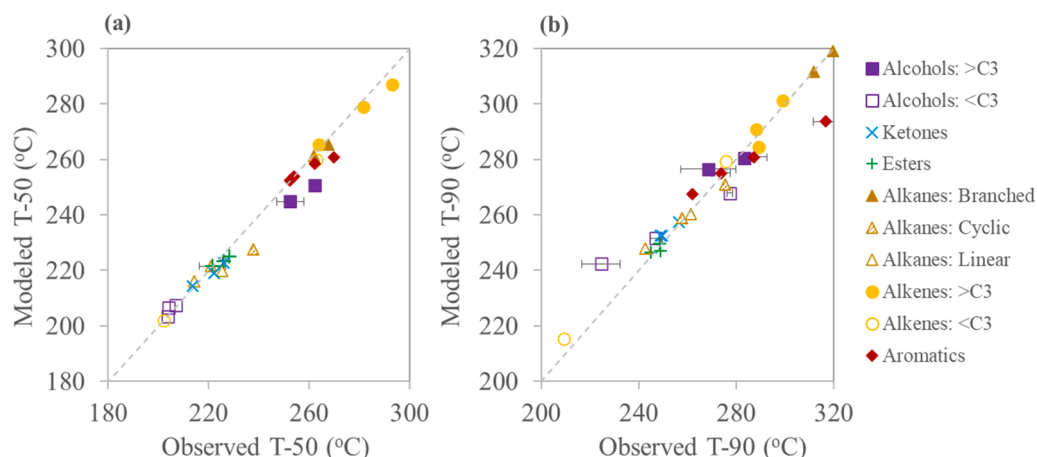


Fig. 4. Model result versus observation for the (a) T-50 s and (b) T-90 s of NMOG light off. The dashed line represents the equivalence line where the modeled result would exactly match the observation. Error bars represent ± 1 standard deviation of the observed values.

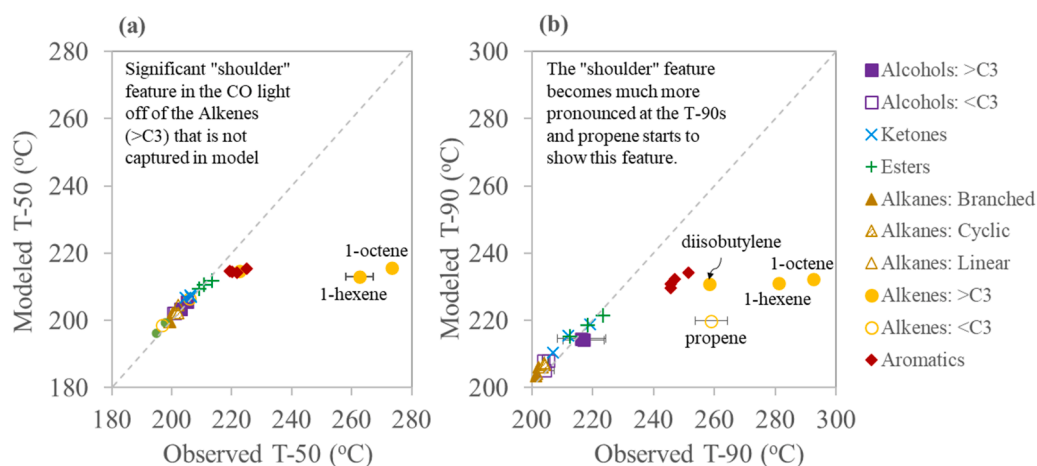


Fig. 5. Model result versus observation for the (a) T-50 s and (b) T-90 s of CO light off. The dashed line represents the equivalence line where the modeled result would exactly match the observation. Error bars represent ± 1 standard deviation of the observed values.

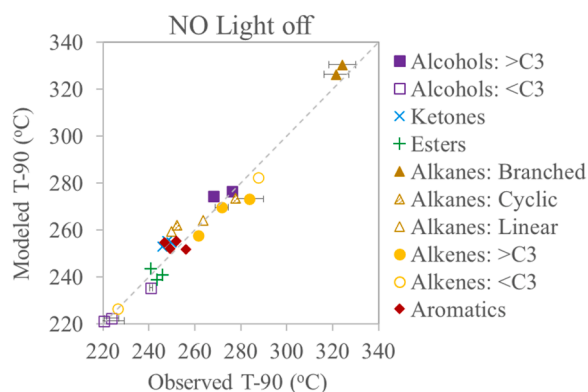


Fig. 6. Model result versus observation for the (a) T-50 s and (b) T-90 s of NO light off. The dashed line represents the equivalence line where the modeled result would exactly match the observation. Error bars represent ± 1 standard deviation of the observed values.

significantly weaker as both the temperature rises and as the HC is consumed (because the adsorption binding affinity decreases exponentially with temperature). Under these conditions, it would be expected that the CO conversion to remain very low at low temperatures and low HC conversion, then increase dramatically as temperature and HC

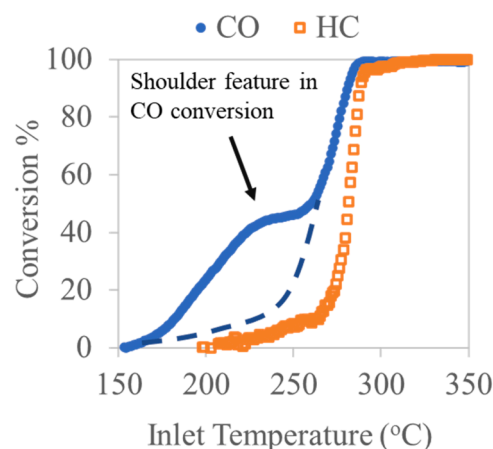


Fig. 7. CO and HC conversions as a function of temperature for the 1-hexene light-off experiments. The dashed line qualitatively represents an expected result of CO light off if the only mechanism impacting the elevated CO light-off temperature were caused by inhibition from HCs.

conversion both increase. However, this is not what is observed in these cases, as demonstrated in Fig. 7 for 1-hexene light off.

Fig. 7 shows the data for the CO and HC light off for the 1-hexene data set. The CO conversion profile shows that 40 % CO conversion is achievable at around 220 °C, but that getting to 50 % CO conversion requires a temperature above 260 °C. This results in a significant shoulder feature in the CO light off where CO actually starts to light off early, but then slows down significantly before fully converting. If this effect were caused by simple HC inhibition, then one would expect the CO light off would follow a profile as shown by the dashed in Fig. 7, where at low temperatures and low HC conversion (i.e., high HC concentrations) the impact of HC inhibition would be greatest and thus would see the greatest losses in CO conversion. Instead, what is observed is that CO light off behaves initially as though it were not inhibited (from 150 to 210 °C), then later behaves as though it is becoming inhibited (from 210 to 250 °C), before finally fully converting above 260 °C.

What is clear from these results is that the global reaction mechanisms explored in this work may be missing some key reaction pathways associated with the CO light off. Additionally, those associated pathways that give rise to the shoulder feature seen in Fig. 7 are only pronounced for specific molecular groups, namely large Alkenes, Aromatics, and propene. Thus, the HC must be involved in some manner that would have resulted in the shift in CO conversion, but that involvement would not necessarily be through inhibition alone for reasons discussed previously. It is also worth noting that this observed shoulder would not likely be the result of oxygen deficiencies as there should still be significant oxygen available for CO oxidation in the 210–250 °C window.

A potential way to explain this behavior may be the combination of inhibition effects and partial oxidation or some transformation of the HCs involved. Inhibition occurs when one species binds to an active site more favorably than another species, thus preventing the use of that site for the reaction.[6,13,36–41] If the HCs in question cannot reach the active sites to bind to them, or do not themselves bind with those sites favorably, then there would be little or no inhibition effect on CO light off, as observed in the lower temperature regime (150–210 °C in Fig. 7). As the temperature increases, if the HCs in question begin to partially oxidize and/or break down to form a different subset of HCs that do bond more favorably with the active sites, then that would effectively slow down CO conversion (as seen from 210 to 250 °C in Fig. 7). Further increases in temperature would then cause the oxidation or desorption of this subset of HCs from the active sites and allow CO to react again. This might explain why there is initially no inhibition on CO, followed by a mid-temperature inhibition effect on CO, while the total HCs concentration remains relatively unchanged in this temperature window.

Other literature has also noted a “shoulder” feature or shifts in CO conversion profiles [59,60]. Lang et al. [59] describes this shift as a change in the order of the CO self-inhibition effect where the reaction order would shift from -1 to -0 with the addition of $\text{CeO}_2\text{-ZrO}_2$ in the catalyst. This would suggest a change in the CO conversion mechanism caused by a change in the surface chemistry. Given that the catalyst is zoned, this may imply that each zone of the domain actually needed to have a different reaction pathway and different reaction rates. However, since the data collected in this work was not spatially resolved, it is difficult to make this assertion as the information necessary to resolve the kinetics of each individual zone was not explored in this work.

Spatially resolved CO profiles in the work by Hazlett and Epling [60] shows that this “shoulder” feature appears towards the front half of the catalyst. That feature in the CO profile was attributed to partial oxidation of the HCs resulting in a change in the inhibition effects due to the formation of new intermediate HCs, as we have postulated above. Coupled with the change in CO chemistry with the zoning of the catalyst, this may help provide an explanation to the “shoulder” features we see in a few of the experiments from this work.

4.3. Kinetics evaluation with blends

With the kinetics approximated for all NMOG species, the aim is to make predictions on the light-off characteristics of various fuel blends. The data used for this model analysis comes from Majumdar et al. [30] and the experimental setup that was used is described briefly in Section 2. No model parameters were fitted for this analysis; the only changes to the model were that the total NMOG content would be made from a mixture of different NMOGs in the feed and the inhibition effect from NMOGs (Eq. 2) would be the summation of individual inhibition effects of each fuel in the blend.

The blends/mixtures examined in this work are briefly summarized in Table 5 and exact mixture compositions are provided in Majumdar et al. [30] Many of the fuel blends were based on a surrogate blendstock for oxygenate blending (BOB) containing 55 % iso-octane, 25 % toluene, 15 % n-heptane, and 5 % 1-hexene, by volume. High performance fuel components (i.e., ethanol, diisobutylene, and iso-butanol) were mixed at 10 %, 20 %, and 30 % by volume into the surrogate BOB. In addition to these multicomponent surrogate fuel blends, several binary mixtures were used to investigate the interactions between individual species. One set of binary blends consisted of 50–50 mixtures of iso-octane, toluene, and n-heptane mixed together in equal parts by volume. A second set of binary Toluene-Heptane mixtures combined those two components in volume fractions of 5 %, 10 %, and 25 % toluene mixed with n-heptane. A set of 30–70 mixtures of diisobutylene and ethanol consisted of 30 % diisobutylene or 30 % ethanol mixed with 70 % of either iso-octane, toluene, or n-heptane.

Simulated light-off temperatures for total NMOG, CO, and NO are plotted against the observed light-off temperatures in Figs. 8 through 10, respectively. The full suite of transient simulation results is available in Supplemental Information, Section H. Fig. 8 shows that the total NMOG conversions predicted by the model are generally within 10 °C of the observations for the full data set. This indicates that the relatively simplistic model outlined in this work is adequate for making predictions on the light-off characteristics of total NMOG conversion for a variety of mixtures. The predicted T-50 s for CO light off (Fig. 9-a) are also all within a 10 °C window, although there is a bias in the model that shows the model consistently predicts a lower T-50 than observed in the data. This bias is primarily attributable to the same errors seen for the pure fuels analysis of the CO light off (Fig. 5), and tends to make the predictions worse for the T-90 s (Fig. 9-b). Additionally, as the proportion of the fuel blend includes higher levels of toluene (Aromatics) and

Table 5
Summary of Blendstocks Examined in this Work.

Mixture Group/Name	Compositions (vol %)
50–50 Mixtures	50 % iso-octane; 50 % heptane 50 % iso-octane; 50 % toluene 50 % toluene; 50 % heptane
Toluene-Heptane Mixtures	25 % toluene; 75 % heptane 10 % toluene; 90 % heptane 5 % toluene; 95 % heptane
30–70 Diisobutylene Mixtures	30 % diisobutylene; 70 % iso-octane 30 % diisobutylene; 70 % heptane 30 % diisobutylene; 70 % toluene
30–70 Ethanol Mixtures	30 % ethanol; 70 % iso-octane 30 % ethanol; 70 % heptane 30 % ethanol; 70 % toluene
Baseline BOB	55 % iso-octane; 25 % toluene; 15 % heptane; 5 % hexene
Ethanol/BOB Blends	10 % ethanol + 90 % Baseline BOB 20 % ethanol + 80 % Baseline BOB 30 % ethanol + 70 % Baseline BOB
Diisobutylene/BOB Blends	10 % diisobutylene + 90 % Baseline BOB 20 % diisobutylene + 80 % Baseline BOB 30 % diisobutylene + 70 % Baseline BOB
Isobutanol/BOB Blends	10 % isobutanol + 90 % Baseline BOB 20 % isobutanol + 80 % Baseline BOB 30 % isobutanol + 70 % Baseline BOB

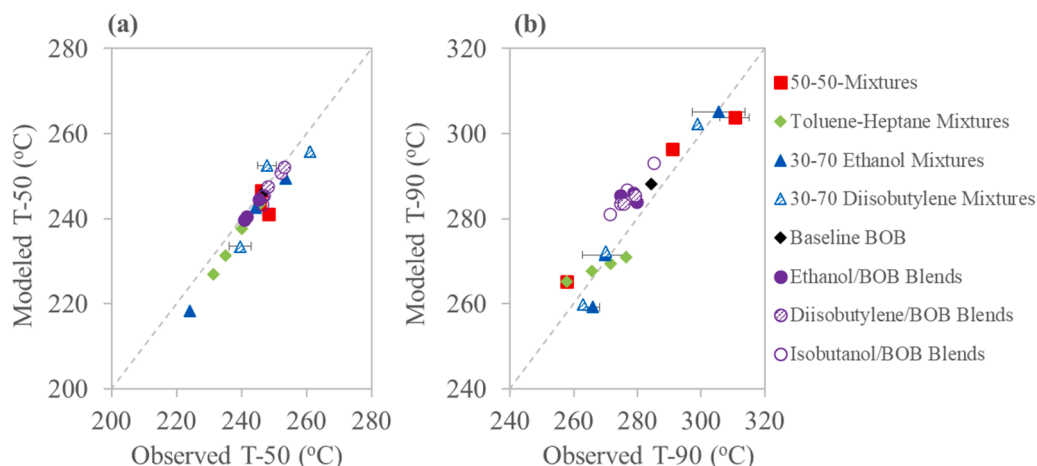


Fig. 8. Model prediction versus observation for the (a) T-50 s and (b) T-90 s of the total mixed/blended NMOG light off. The dashed line represents the equivalence line where the modeled result would exactly match the observation. Error bars represent ± 1 standard deviation of the observed values.

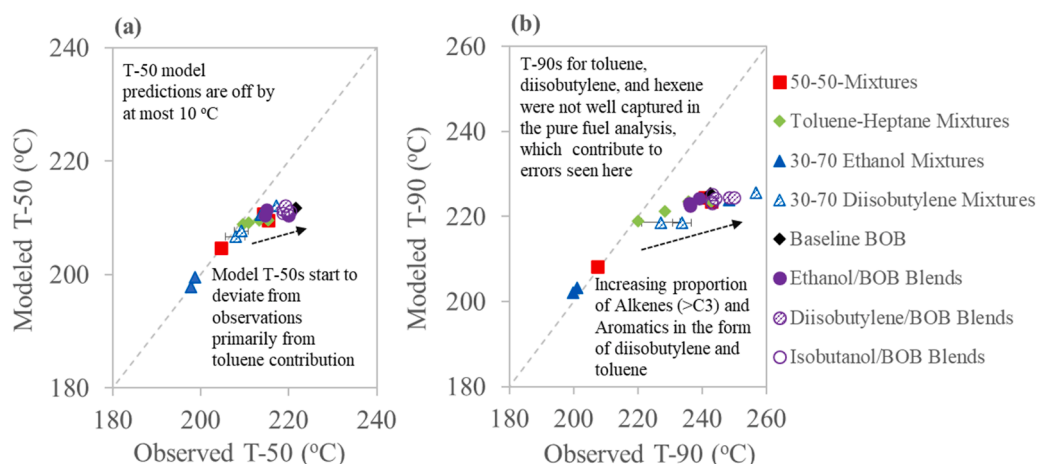


Fig. 9. Model prediction versus observation for the (a) T-50 s and (b) T-90 s of CO light off from blends. The dashed line represents the equivalence line where the modeled result would exactly match the observation. Error bars represent ± 1 standard deviation of the observed values.

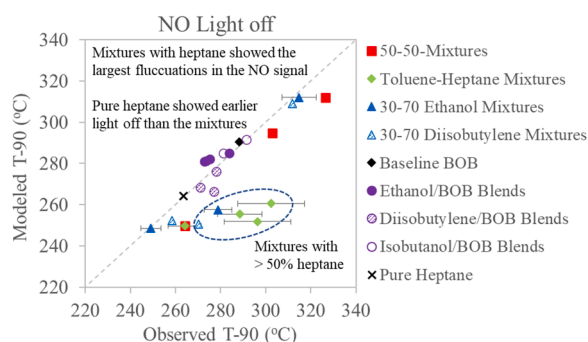


Fig. 10. Model prediction versus observation for the (a) T-50 s and (b) T-90 s of NO light off from blends. The dashed line represents the equivalence line where the modeled result would exactly match the observation. Error bars represent ± 1 standard deviation of the observed values. The 'x' on the plot shows what the result from 100 % n-heptane is as a point of comparison between the other n-heptane blends.

diisobutylene (Alkenes with more than 3 carbons), the bias in the model predictions of the CO light-off T-90 s becomes worse (Fig. 11). This brings the discussion back to the shoulder feature observed in the CO light-off profiles for these same molecular groups (Fig. 7). That same

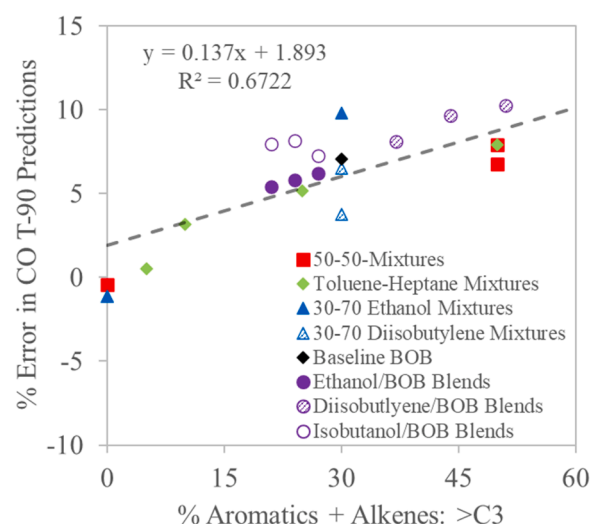


Fig. 11. Plot of model error in the T-90 s for CO light off vs the relative content of the Aromatics and Alkenes (>C3) in the blendstock. This analysis highlights a clear trend in a loss of model accuracy as the Aromatic and Alkene (>C3) content increases, as indicated by the linear regression shown in the dashed line.

feature can be seen in several of the blendstock light-off profiles (Supplemental Information, Section H). As before, it is likely that this feature is the result of intermediate (or partially oxidized) species adsorbing and temporarily blocking the catalyst surface. Since the model does not include intermediate species, this feature is not captured well.

The model predictions for NO light off are a bit of a mixed bag of results. While the majority of the model predictions match the observations within roughly 10 °C, there are a handful of predictions that show a significant negative bias in predicted light-off temperatures. Upon closer inspection, it was observed that all of the mixtures for which the model had under predicted the T-90 s for NO light off contained more than 50 % n-heptane. Initially, it would seem that n-heptane was likely a cause for the depressed T-90 s for NO light off. However, as is shown in Fig. 10, the light-off temperature for 100 % n-heptane (black 'x' mark) is actually significantly lower (and better predicted by the model) than the T-90 for 95 % n-heptane (rightmost green diamond). Additionally, the standard deviations for the T-90 s of the n-heptane mixtures in question are much larger than any other data set (see the tables in Supplemental Information, Section I for full T-n results of mixtures).

Given how much noise was in the NO signals for these experiments, it may be possible that there were undue fluctuations in the vapor delivery system which would have caused the NO conversion to rapidly change and cause significant uncertainty in the actual T-90 s. These fluctuations can be clearly seen in the transient plots (Supplemental Information, Section H) for these > 50 % n-heptane mixtures and are generally not seen in many of the other mixtures. However, this explanation may be insufficient as failures in the vapor delivery system should also be coupled with a loss in NH₃ generation, as the λ value would rise above 1 and excess O₂ would consume H₂ needed to form NH₃. This only appears to be the case for some of the experiments, as indicated in the loss in the bimodal formation nature of NH₃ see in Supplemental Information, Section H. Alternatively, there may also be a change in NO conversion mechanism that this simpler inhibition model does not capture well.

Model results for NH₃ and N₂O formation during light off of pure fuels and the blendstocks are also provided in Supplemental Information (Section E and Section H, respectively). It is worth noting that in all cases, these are pure predictions since no additional mechanisms were introduced for NH₃ or N₂O formation from any HCs and only reactions with CO and H₂ are considered in their formation (Table 2). In general, both NH₃ and N₂O formation were predicted fairly well for the early portions of the light-off curves, but would tend to miss some secondary peaks at higher temperatures. Since those secondary peaks were never observed in the experimental cases done in the absence of HCs (Supplemental Information, Section C), this may indicate that there is a reaction pathway by which HCs may be in some way facilitating NH₃ and/or N₂O formation at higher temperatures.

5. Conclusions

In this work, a set of controlled light-off experiments in the absence of any HCs was performed in order to clearly determine the intrinsic kinetics of CO oxidation, H₂ oxidation, and NO reduction on a commercial, dual-zone Pd/Rh TWC. Those experiments were designed such that each set of global reactions (Table 2) could be independently determined and would supplement HC light-off data from pure fuels and fuel blends from prior literature [29,30]. A simple global kinetics and inhibition model was then developed based on this experimental work and the data collected was used to calibrate that model for the CO, H₂, and NO related reactions.

A core principle of the model development was that fuel components could be sub-divided into a series of molecular groups based on similar reactivities denoted in Majumdar et al. [29] Each NMOG species in those respective groups (Table 4) would have the same kinetic parameters within the global kinetics model, thus significantly reducing the number of parameters needed to make predictions for a given system. This

provides a very computationally efficient means of predicting light-off characteristics for complex exhaust mixtures.

The model was then calibrated to each pure fuel data set and a common set of kinetic parameters for HC light off was determined for each molecular group. The results in Figs. 4 through 6 show that this model paradigm does very well to capture the light-off characteristics of most of the fuel components analyzed. However, the Aromatics and larger Alkenes (those with more than 3 carbons) did show some significant errors in the CO light off. This error was traced back to a "shoulder" feature that is unique to these HCs (Fig. 7) and could not be explained by simple inhibition alone. Thus, some additional mechanism in the set of reactions considered in this work would need to be added to capture this feature.

The calibrated model was then used to make predictions on the light-off characteristics of a number of blends studied from Majumdar et al. [30] Discounting the T-90 s for NO light off of high n-heptane content mixtures, the model worked relatively well to predict the light-off characteristics for each blend (Figs. 8 through 10). The errors observed from the T-90 s for CO light off were to be expected as they resulted from model errors associated with CO light off for Aromatics and larger alkenes from the prior analysis with the pure fuels light-off experiments (Fig. 5). This demonstrates the applicability of simple, global kinetics models for more complex fuel blends and shows that these reduced-order type of inhibition models may be useful as a first approximation to light-off behavior of future fuel blends or formulations.

CRedit authorship contribution statement

Austin Ladshaw: Visualization, Formal analysis, Conceptualization, Methodology, Software, Visualization, Formal analysis. **Sreshtha Sinha Majumdar:** Conceptualization, Methodology, Project administration, Validation, Writing – review & editing. **Josh A. Pihl:** Data curation, Resources, Supervision, Funding acquisition, Project administration, Supervision, Writing – review & editing.

Declaration of Competing Interest

The authors declare that they have no known competing financial interests or personal relationships that could have appeared to influence the work reported in this paper.

Data Availability

Data will be made available on request.

Acknowledgements

This research was supported by the DOE Office of Energy Efficiency and Renewable Energy (EERE), Bioenergy Technologies Office (BETO), and Vehicle Technologies Office (VTO) under the DOE Co-Optimization of Fuels and Engines Initiative and used resources at the National Transportation Research Center, a DOE-EERE User Facility at Oak Ridge National Laboratory. The authors gratefully acknowledge the support and direction of Kevin Stork at VTO, Alicia Lindauer at BETO, and the Co-Optima Leadership Team.

Notice

This manuscript has been authored by UT-Battelle, LLC under Contract No. DE-AC05-00OR22725 with the U.S. Department of Energy. The United States Government retains and the publisher, by accepting the article for publication, acknowledges that the United States Government retains a non-exclusive, paid-up, irrevocable, world-wide license to publish or reproduce the published form of this manuscript, or allow others to do so, for United States Government purposes. The

Department of Energy will provide public access to these results of federally sponsored research in accordance with the DOE Public Access Plan (<http://energy.gov/downloads/doe-public-access-plan>).

Appendix A. Supporting information

Supplementary data associated with this article can be found in the online version at [doi:10.1016/j.apcatb.2022.122281](https://doi.org/10.1016/j.apcatb.2022.122281).

References

- [1] J. Wang, H. Chen, Z. Hu, M. Yao, Y. Li, A review on the Pd-Based three-way catalyst, *Cat. Rev. Sci. Eng.* 57 (2015) 79–144, <https://doi.org/10.1080/01614940.2014.977059>.
- [2] H.J. Kwon, J.H. Baik, Y.T. Kwon, I.S. Nam, S.H. Oh, Detailed reaction kinetics over commercial three-way catalysts, *Chem. Eng. Sci.* 62 (2007) 5042–5047, <https://doi.org/10.1016/j.ces.2007.01.082>.
- [3] R. Möller, C.H. Onder, L. Guzzella, M. Votsmeier, J. Gieshoff, Analysis of a kinetic model describing the dynamic operation of a three-way catalyst, *Appl. Cat. B: Environ.* 70 (2007) 269–275, <https://doi.org/10.1016/j.apcatb.2005.12.022>.
- [4] R.E. Hayes, L.S. Mukadi, M. Votsmeier, J. Gieshoff, Three-way catalytic converter modelling with detailed kinetics and washcoat diffusion, *Top. Catal.* 30 (2004) 411–415, <https://doi.org/10.1023/B:TOCA.0000029783.16199.f3>.
- [5] J. Gong, C. Rutland, Three way catalyst modeling with ammonia and nitrous oxide kinetics for a lean burn spark ignition direct injection (SIDI) gasoline engine, *SAE Tech. Pap.* (2013) 01–1572, <https://doi.org/10.4271/2013-01-1572>.
- [6] D. Shah, K. Premchand, D. Pedro, Control oriented physics based three-way catalytic converter temperature estimation model for real time controllers, *SAE Tech. Pap.* (2020) 01–0904, <https://doi.org/10.4271/2020-01-0904>.
- [7] D. Linder, L. Musmann, J.A.A. van den Tillaart, E.S. Lox, A. Roshan, G. Garr, R. Reason, Comparison of Pd-only, Pd/Rh, and Pt/Rh catalysts in TLEV, LEV vehicle applications - real vehicle data versus computer modeling results, *SAE Tech. Pap.* (2000) 01–0501, <https://doi.org/10.4271/2000-01-0501>.
- [8] D. Wang, J. Gong, J. Luo, J. Li, K. Kamasamudram, N. Currier, A. Yezzerets, Distinct reaction pathways for methane oxidation on different oxidation states over Pd-based three-way catalyst (TWC), *Appl. Cat. A: Gen.* 572 (2019) 44–50, <https://doi.org/10.1016/j.apcata.2018.12.022>.
- [9] P. Granger, C. Dujardin, J.F. Paul, G. Leclercq, An overview of kinetic and spectroscopic investigations on three-way catalysts: mechanistic aspects of the CO + NO and CO + N₂O, *React., J. Mol. Cat. A: Chem.* 228 (2005) 241–253, <https://doi.org/10.1016/j.molcata.2004.09.081>.
- [10] C. McAtee, G. McCullough, D. Sellick, A. Goguet, Characterization and modelling of the reactions in a three-way Pd/Rh catalyst in the exhaust gas from an ethanol-fueled spark-ignition engine, *Proc. Inst. Mech. Eng. Part D: J. Automob. Eng.* 233 (2019) 3222–3234, <https://doi.org/10.1177/0954407018821031>.
- [11] R.H. Nibbelke, A.J.L. Nievergeld, J.H.B.J. Hoebink, G.B. Marin, Development of a transient kinetic model for the CO oxidation by O₂ over a Pt/Rh/CeO₂/γ-Al₂O₃ three-way catalyst, *Appl. Cat. B: Environ.* 19 (1998) 245–259, [https://doi.org/10.1016/S0926-3373\(98\)00076-9](https://doi.org/10.1016/S0926-3373(98)00076-9).
- [12] R. Rajasree, J.H.B.J. Hoebink, J.C. Schouten, Transient kinetics of carbon monoxide oxidation by oxygen over supported palladium/ceria/zirconia three-way catalysts in the absence and presence of water and carbon dioxide, *J. Catal.* 223 (2004) 36–43, <https://doi.org/10.1016/j.jcat.2003.12.014>.
- [13] X. Yan, R. Sone, R. Inoue, J. Kusaka, K. Umezawa, Y. Kondo, 2019. Modeling three-way catalyst converters during cold starts and potential improvements, *SAE Technical Paper* 2019-01-2326, 2019. <https://doi.org/10.4271/2019-01-2326>.
- [14] Y. Toya, H. Nakayama, H. Hara, M. Nagata, 2019. “Optimization of TWC Design for Various Engine Operation Conditions”, *SAE Technical Paper* 2019-01-1290, 2019. <https://doi.org/10.4271/2019-01-1290>.
- [15] Y. Xi, N. Ottinger, Z. Liu, The dynamics of methane and NO_x removal by a three-way catalyst: a transient response study, *SAE Int. J. Engines* 11 (2018) 1331–1341, <https://doi.org/10.4271/2018-01-1270>.
- [16] T. Khossusi, R. Douglas, G. McCullough, 2003. Development and validation of an oxygen storage model for three way catalysts, *SAE Technical Paper* 2003-32-0060, 2003. <https://doi.org/10.4271/2003-32-0060>.
- [17] A. Simson, K. Roark, R. Farrauto, A feasibility study of niobium-containing materials for oxygen storage in three way catalytic converters, *Appl. Cat. B: Environ.* 159 (2014) 106–111, <https://doi.org/10.1016/j.apcatb.2014.04.006>.
- [18] J. Rink, N. Meister, F. Herbst, M. Votsmeier, Oxygen storage in three-way-catalysts is an equilibrium controlled process: experimental investigation of the redox thermodynamics, *Appl. Cat. B: Environ.* 206 (2017) 104–114, <https://doi.org/10.1016/j.apcatb.2016.12.052>.
- [19] J. Wu, J.P. Dacquain, N. Djelal, C. Cordier, C. Dujardin, P. Granger, Calcium and copper substitution in stoichiometric and La-deficient LaFeO₃ compositions: a starting point in next generation of three-way-catalysts for gasoline engines, *Appl. Cat. B: Environ.* 282 (2021), 119621, <https://doi.org/10.1016/j.apcatb.2020.119621>.
- [20] S. Nandi, J.X. Wu, P. Simon, N. Nuns, M. Trentesaux, A. Tougeri, E. Fonda, J. S. Girardon, J.F. Paul, A.S. Mamede, E. Berrier, Mn- or Cu- substituted LaFeO₃-based three-way catalysts: highlighting different catalytically operating modes of La_{0.67}Fe_{0.8}Mn_{0.2}O₃ (M=Cu, Mn), *Appl. Cat. B: Environ.* 296 (2021), 120330, <https://doi.org/10.1016/j.apcatb.2021.120330>.
- [21] X. Yao, Q. Yu, Z. Ji, Y. Lv, Y. Cao, C. Tang, F. Gao, L. Dong, Y. Chen, A comparative study of different doped metal cations on the reduction, adsorption and activity of CuO/CeO₂/MnO₂/ZrO₂ (M=Zr⁴⁺, Sn⁴⁺, Ti⁴⁺) catalysts for NO+CO reaction, *Appl. Cat. B: Environ.* 131 (2013) 293–304, <https://doi.org/10.1016/j.apcatb.2012.11.020>.
- [22] J.C.P. Jones, J.B. Roberts, J. Pan, R.A. Jackson, 1999. Modeling the transient characteristics of a three-way catalyst, *SAE Technical Paper* 1999-01-0460, 1999. <https://doi.org/10.4271/1999-01-0460>.
- [23] J. Le Louvetel-Polloy, S. Balaji, F. Lafossas, 2019. Development of Three Way Catalyst Aging Model: Application to Real Driving Emission Condition, *SAE Technical Paper* 2019-24-0047, 2019. <https://doi.org/10.4271/2019-24-0047>.
- [24] S.A. Malamis, M. Li, W.S. Epling, M.P. Harold, Steady state and lean-rich cycling study of a three-way NO_x storage catalyst: experiments, *Appl. Cat. B: Environ.* 237 (2018) 588–602, <https://doi.org/10.1016/j.apcatb.2018.06.001>.
- [25] J. Pihl, J. Thomas, S. Sinha Majumdar, S. Huff, B. West, T. Toops, Development of a cold start fuel penalty metric for evaluating the impact of fuel composition changes on SI engine emissions, *Control, SAE Tech. Pap.* (2018) 01–1264, <https://doi.org/10.4271/2018-01-1264>.
- [26] J.M.A. Harmsen, 2001. Kinetic modelling of the dynamic behavior of an automotive three-way catalyst under cold-start conditions, PhD Thesis, Technische Universiteit, 2001. <https://doi.org/10.6100/IR547637>.
- [27] T. Bärthel, A. Drochner, H. Vogel, M. Votsmeier, Effect of diverse hydrocarbons on the cold start behavior of three-way catalysts, *Top. Catal.* 60 (2017) 278–282, <https://doi.org/10.1007/s11244-016-0609-8>.
- [28] M.S. Reiter, K.M. Kockelman, The problem of cold starts: a closer look at mobile source emissions levels, *Trans. Res. Part D Transp. Environ.* 43 (2016) 123–132, <https://doi.org/10.1016/j.trd.2015.12.012>.
- [29] S.S. Majumdar, J.A. Pihl, T.J. Toops, Reactivity of novel high-performance fuels on commercial three-way catalysts for control of emissions from spark-ignition engines, *Appl. Energy* 255 (2019), 113640, <https://doi.org/10.1016/j.apenergy.2019.113640>.
- [30] S.S. Majumdar, J.A. Pihl, Impact of selected high-performance fuel blends on three-way catalyst light off under synthetic spark-ignition engine-exhaust conditions, *Energy Fuels* 34 (2020) 12900–12910, <https://doi.org/10.1021/acs.energyfuels.0c02102>.
- [31] V. Kärcher, P. Hellier, N. Ladommatos, 2019. Effects of exhaust gas hydrogen addition and oxygenated fuel blends on the light-off performance of a three-way catalyst, *SAE Technical Paper* 2019-01-2329, 2019. <https://doi.org/10.4271/2019-01-2329>.
- [32] R.L. McCormick, G. Fioroni, L. Fouts, E. Christensen, J. Yanowitz, E. Polikarpov, K. Albrecht, D.J. Gaspar, J. Gladden, A. George, Selection criteria and screening of potential biomass-derived streams as fuel blendstocks for advanced spark-ignition engines, *SAE Int. J. Fuels Lubr.* 10 (2017) 442–460, <https://doi.org/10.4271/2017-01-0868>.
- [33] K.G. Rappé, C. DiMaggio, J.A. Pihl, J.R. Theis, S.H. Oh, G.B. Fisher, J. Parks, V. G. Easterling, M. Yang, M.L. Stewart, K.C. Howden, Aftertreatment protocols for catalyst characterization and performance evaluation: low-temperature oxidation, storage, three-way, and NH₃-SCR catalyst test protocols, *Emiss. Control Sci. Technol.* 5 (2019) 183–214, <https://doi.org/10.1007/s40825-019-00120-7>.
- [34] P.M. Laing, M.D. Shane, S. Son, A.A. Adamczyk, P. Li, A simplified approach to modeling exhaust system emissions: SIMTWC, *SAE Tech. Pap.* (1999) 01–3476, <https://doi.org/10.4271/1999-01-3476>.
- [35] L. Glielmo, S. Santini, M. Milano, 2000. Three-way catalytic converter modelling: Neural Networks and Genetic Algorithms for the reaction kinetics submodel, *SAE Technical Paper* 2000-01-0212, 2000. <https://doi.org/10.4271/2000-01-0212>.
- [36] K. Ohsawa, N. Baba, S. Kojima, Numerical prediction of transient conversion characteristics in a three-way catalytic converter, *SAE Technical Paper Series* 982556, 1998. <https://doi.org/10.4271/982556>.
- [37] S. Buchner, S.S. Lardies, A. Degen, A. Donnerstag, W. Held, 2000. A modular numerical simulation tool predicting catalytic converter light-off by improved modeling of thermal management and conversion characteristics, *SAE Technical Paper* 2001-01-0940, 2000. <https://doi.org/10.4271/2001-01-0940>.
- [38] S.K. Rao, R. Imam, K. Ramanathan, S. Pushpavanam, Sensitivity analysis and kinetic parameter estimation in a three way catalytic converter, *Ind. Eng. Chem. Res.* 48 (2009) 3779–3790, <https://doi.org/10.1021/ie801244w>.
- [39] C. Dubien, D. Schweich, G. Mabilon, B. Martin, M. Prigent, Three-way catalytic converter modelling: fast- and slow-oxidizing hydrocarbons, inhibiting species, and steam-reforming reaction, *S., Chem. Eng. Sci.* 3 (1998) 471–481, [https://doi.org/10.1016/S0009-2509\(97\)00313-8](https://doi.org/10.1016/S0009-2509(97)00313-8).
- [40] K. Ramanathan, C.S. Sharma, Kinetic parameter estimation for three way catalyst modeling, *Ind. Eng. Chem. Res.* 50 (2011) 9960–9979, <https://doi.org/10.1021/ie200726j>.
- [41] L.P. Ma, H.J. Bart, P. Ning, A. Zhang, G. Wu, Z. Zengzang, Kinetic study of three-way catalyst of automotive exhaust gas: Modeling and application, *Chem. Eng. J.* 155 (2009) 241–247, <https://doi.org/10.1016/j.cej.2009.07.045>.
- [42] J. Braun, T. Hauber, H. Tobben, P. Zacke, D. Chatterjee, O. Deutschmann, J. Warnatz, Influence of physical and chemical parameters on the conversion rate of a catalytic converter: a numerical simulation study, *SAE Technical Paper* 2000-01-0211, 2000. <https://doi.org/10.4271/2000-01-0211>.
- [43] M. Chen, J. Aleixo, S. Williams, T. Leprince, Y. Yong, CFD modelling of 3-way catalytic converters with detailed catalytic surface reaction mechanism, *SAE Tech. Pap.* 2004 (2004) 01–0148, <https://doi.org/10.4271/2004-01-0148>.
- [44] D. Chatterjee, O. Deutschmann, J. Warnatz, Detailed surface reaction mechanism in a three-way catalyst, *Faraday Discuss.* 119 (2001) 371–384, <https://doi.org/10.1039/B101968F>.

- [45] P. Koci, M. Kubicek, M. Marek, Modeling of three-way catalyst monolith converters with microkinetics and diffusion in the washcoat, *Ind. Eng. Chem. Res.* 43 (2004) 4503–4510, <https://doi.org/10.1021/ie034137k>.
- [46] S.E. Voltz, C.R. Morgan, D. Liederman, S.M. Jacob, Kinetic study of carbon monoxide and propylene oxidation on platinum catalysts, *Ind. Eng. Chem. Prod. Res. Dev.* 12 (1973) 294–301, <https://doi.org/10.1021/i360048a006>.
- [47] B. Subramaniam, A. Varma, Reaction kinetics on a commercial three-way catalyst: the CO-NO-O₂-H₂O system, *Ind. Eng. Chem. Prod. Res. Dev.* 24 (1985) 512–516, <https://doi.org/10.1021/i300020a005>.
- [48] S. Tischer, Y. Jiang, K.W. Hughes, M.D. Patil, M. Murtagh, Three-way-catalyst modeling - A comparison of 1D and 2D simulations, *SAE Technical Paper 2007-01-1071*, 2007. <https://doi.org/10.4271/2007-01-1071>.
- [49] J.A. Botas, M.A. Gutierrez-Ortiz, M.P. Gonzalez-Marcos, J.A. Gonzalez-Marcos, J. R. Gonzalez-Velasco, Kinetic considerations of three-way catalysis in automobile exhaust converters, *Appl. Cat. B: Environ.* 32 (2001) 243–256, [https://doi.org/10.1016/S0926-3373\(01\)00144-8](https://doi.org/10.1016/S0926-3373(01)00144-8).
- [50] A. Ladshaw, J.A. Pihl, Measurement and Modeling of the effects of exhaust composition and hydrothermal aging on the ammonia storage capacity of a commercial Cu-SSZ-13 catalyst, *Appl. Cat. B: Environ.* 303 (2022), 120898, <https://doi.org/10.1016/j.apcatb.2021.120898>.
- [51] I. Nova, D. Bounechada, R. Maestri, E. Tronconi, A.K. Heibel, T.A. Collins, T. Boger, Influence of the substrate properties on the performance of NH₃-SCR monolithic catalysts for the aftertreatment of diesel exhaust: an experimental and modeling study, *Ind. Eng. Chem. Res.* 50 (2011) 299–309, <https://doi.org/10.1021/ie1015409>.
- [52] A. Ladshaw, 2022. CATS: Catalytic After Treatment System, <https://github.com/aladshaw3/cats> (Accessed 19 January 2022).
- [53] E.S. Domaiski, E.D. Hearing, Estimation of the thermodynamic properties of hydrocarbons at 298.15 K, *J. Phys. Chem. Ref. Data* 17 (1988) 1637–1678, <https://doi.org/10.1063/1.555814>.
- [54] C.J. Permann, D.R. Gaston, D. Andr s, R.W. Carlsen, F. Kong, A.D. Lindsay, J. M. Miller, J.W. Peterson, A.E. Slaughter, R.H. Stogner, R.C. Martineau, MOOSE: enabling massively parallel multiphysics simulation, *SoftwareX* 11 (2020), 100430, <https://doi.org/10.1016/j.softx.2020.100430>.
- [55] B. Riviere, Discontinuous Galerkin methods for solving elliptic and parabolic equations: theory and implementation, *SIAM, Phila.* (2008), <https://doi.org/10.1137/1.9780898717440>.
- [56] D.A. Knoll, D.E. Keyes, Jacobian-Free Newton-Krylov methods: a survey of approaches and applications, *J. Comp. Phys.* 193 (2004) 357–397, <https://doi.org/10.1016/j.jcp.2003.08.010>.
- [57] A. W chter, L.T. Biegler, On the implementation of an interior-point filter line-search algorithm for large-scale nonlinear programming, *Math. Prog.* 106 (2006) 25–57, <https://doi.org/10.1007/s10107-004-0559-y>.
- [58] M.J. Patterson, D.E. Angove, N.W. Cant, The effect of carbon monoxide on the oxidation of four C6 to C8 hydrocarbons over platinum, palladium and rhodium, *Appl. Cat. B: Environ.* 26 (2000) 47–57, [https://doi.org/10.1016/S0926-3373\(00\)00110-7](https://doi.org/10.1016/S0926-3373(00)00110-7).
- [59] W. Lang, P. Laing, Y. Cheng, C. Hubbard, M.P. Harold, Co-oxidation of CO and propylene on Pd/CeO₂-ZrO₂ and Pd/Al₂O₃ monolith catalysts: a light-off, kinetics, and mechanistic study, *Appl. Cat. B: Environ.* 218 (2017) 430–442, <https://doi.org/10.1016/j.apcatb.2017.06.064>.
- [60] M.J. Hazlett, W.S. Epling, Spatially resolving CO and C₃H₆ oxidation reactions in a Pt/Al₂O₃ model oxidation catalyst, *Catal. Today* 267 (2016) 157–166, <https://doi.org/10.1016/j.cattod.2015.11.033>.